A Novel Mixed-bouncing Beam Domain Channel Model for Massive MIMO Communication Systems at mmWave Bands

Hao Qian, Yang Liu*, Cheng-Xiang Wang*, *Fellow, IEEE*, Rui Feng, Wen-Jun Lu, *Senior Member, IEEE*, and Hong-Bo Zhu, *Member, IEEE*.

***Abstract*—Massive multiple-input multiple-output (MIMO), combined with millimeter-wave (mmWave) is a promising solution for the sixth generation (6G) communication systems. Due to numerous obstacles in rich scattering environments, the massive MIMO in the beam domain at mmWave bands exhibit complex characteristics that have not been taken into account in previous studies. In this paper, a novel beam domain channel model (BDCM) with mixed-bouncing clusters for massive MIMO scenarios at mmWave bands is proposed. In this proposed BDCM, the line-of-sight (LoS) ray, single bouncing ray, and double-bouncing ray are simultaneously considered. Moreover, the non-stationarity of the propagation channel is modeled by determining visibility regions (VRs) of the single-bouncing and double-bouncing clusters, respectively. Based on this proposed model, the spatial-temporal correlation function (ST-CF) is obtained and simulated results show that the single-bouncing clusters make a significant contribution on the ST-CF. Finally, impact of the single-bouncing clusters on the other statistical property, such as channel capacity, is also presented. Results suggest that ignoring the non-stationarity and power contribution of the single-bouncing rays may lead to inaccurate evaluation of the channel capacity. The proposed model may be used in the 6G massive MIMO communication systems at mmWava bands.**

***Index Terms*—BDCM, mmWave band, 6G, cluster-based model, statistical properties.**

This work was supported by the National Natural Science Foundation of China (NSFC) under Grant 61960206006, the Key Technologies R&D Program of Jiangsu (Prospective and Key Technologies for Industry) under Grants BE2022067, BE2022067-1, and BE2022067-2, the EU H2020 RISE TESTBED2 project under Grant 872172, and the open research fund of Key Lab of Broadband Wireless Communication and Sensor Network Technology (Nanjing University of Posts and Telecommunications, Ministry of Education). (*Corresponding authors: Yang Liu and Cheng-Xiang Wang*.)

H. Qian and Y. Liu are with the School of Internet of Things Engineering, Jiangnan University, Wuxi 214122, China, and also with the Key Lab of Broadband Wireless Communication and Sensor Network Technology (Nanjing University of Posts and Telecommunications, Ministry of Education), Nanjing 210023, China (E-mail: qh971130@163.com and ly71354@163.com).

C.-X. Wang is with the National Mobile Communications Research Laboratory, School of Information Science and Engineering, Southeast University, Nanjing 210096, China, and also with the Purple Mountain Laboratories, Nanjing 211111, China (E-mail: chxwang@seu.edu.cn).

R. Feng is with Purple Mountain Laboratories, Nanjing, 211111, China, and also with the School of Information Science and Engineering, Southeast University, Nanjing, 210096, China (e-mail: fengxiurui604@163.com).

W.-J. Lu and H.-B. Zhu are with Department of Jiangsu Key Laboratory of Wireless Communications, Nanjing University of Posts and Telecommunications, Xinmofan Road 66, Nanjing 210003, China, and also with the Key Laboratory of Wireless Sensor Network Communication, Shanghai Instituteof Microsystem and Information Technology, Chinese Academy of Sciences,865 Changning Road, Shanghai 200050, China (E-mail: wjlu@njupt.edu.cn and zhb@njupt.edu.cn).

I. Introduction

MASSIVE mutiple-input multiple-output (MIMO) technology at millimeter wave (mmWave) band plays a crucial role in sixth generation (6G) communication systems with improved data transmission rates, channel capacity, and spectrum efficiency [1]-[5]. By converting the massive MIMO channels from the spatial domain to the beam domain, the unaffordable hardware cost and power consumption in conventional massive MIMO systems can be solved [6]-[8]. The key technique of beam domain is to uniformly sample the spatial domain [9]. The less directive beams can significantly reduce the effective massive MIMO size and the number of associated RF chains [10]. Moreover, adaptive beamforming techniques, which generate narrow beams in specific directions to ensure higher throughput and better energy efficiency, can be used to overcome the higher path loss and higher penetration loss at the mmWave band [11]. With the narrowed beam width, inter-user interference is mitigated, and opportunities for eavesdropping are reduced, which can be widely applied in future 6G systems [12]-[14]. However, the rich scattering environment can block mmWave signals, resulting in severe channel non-stationarity and dense multipath effects. Thus, it is essential to study the scattering characteristics for massive MIMO at 6G mmWave band in the beam domain channels.

The first beam domain channel model (BDCM) can be traced back to 2013 [15], and a prototype continuous aperture phased (CAP) MIMO beam domain system is used in [16] to conduct the first multi-beam MIMO system measurement at 28 GHz. In these models, the beamforming is accomplished by a lensed antenna array, concentrating signal power from different directions onto different antennas. In recent years, the on-beam domain implementations have been modeled in several aspects such as secret key generation [17], co-time co-frequency uplink and downlink (CCUD) transmission [18]. These models are based on the existing basis expansion model without considering clusters in the environment. Generally, the existing BDCMs are developed based on geometric-based stochastic models (GBSM) and can be summarized into two types. The first type is developed based on single-bouncing GBSM. Propagation neglecting double-bouncing rays is divided into line-of-sight (LoS) and non-line-of-sight (NLoS). These models possess lower computational complexity [19]. The second type is based on double-bouncing GBSM. In these models, the multi-bouncing rays can be characterized sufficiently by adjusting the twin-clusters [20]. But, extensive channel measurements show that there is the coexistence of the single-bouncing and multi-bouncing rays in a number of propagation scenarios [21], [22]. Unfortunately, double-bouncing clusters cannot characterize the single-bouncing rays accurately. This is because the correlation between the angle of arrival (AoA) and angle of departure (AoD) cannot be described even if ignoring the virtual link. Therefore, the single-bouncing and double-bouncing clusters should be simultaneously considered in the channel models. However, to the best of the authors' knowledge, the BDCM that can model both the single-bouncing rays and the double-bouncing rays is still missing.

To fulfill this gap, a novel BDCM with mixed-bouncing clusters is proposed, where the single-bouncing cluster and double-bouncing cluster are generated respectively. The main contributions and innovations of this paper can be summarized as follows.

1) A novel mixed-bouncing BDCM, where the LoS ray, single-bouncing rays, and double-bouncing rays are considered simultaneously, is proposed in this paper. The channel non-stationarity is also modeled by determining the visibility regions (VRs) of the single-bouncing and double-bouncing clusters, respectively. Extensive channel measurements show the accuracy of the proposed model.

2) Based on this proposed model, the spatial-temporal correlation function (ST-CF) of the beam-domain channel is derived and Monte-Caro simulations verify accuracy the derivations. Moreover, simulated results explore the impact of the power ratio and variable VRs of the single-bouncing clusters on the ST-CFs.

3) Impact of the single-bouncing clusters on the channel capacity is analyzed for the first time. Simulated results suggest that ignoring both the VRs and power contributions of the single-bouncing clusters may lead to inaccurate evaluation of the channel capacity.

The rest of this paper is organized as follows. Section II briefly reviews the related works on BDCM. Section III gives the novel BDCM based on the GBSM and the cluster-based channel model. Statistical properties of the proposed model are derived in Section IV. Results and analysis are presented in Section V. Finally, conclusions are drawn in Section VI.

Notation : $|\cdot|$ means absolute value, $||\cdot||$ means length of a vector, $(\cdot)^*$, $(\cdot)^T$, $(\cdot)^H$ mean complex conjugation, transpose, and conjugate transpose operations, respectively, $det\left(\cdot\right)$ means determinant operator, $\odot$ and $\otimes$ mean Schur-Hadamard (element-wise) product and Kronecker product, respectively, $\mathbb{E}\{\cdot\}$ accounts for statistical average.

II. Related works

In the past decades, scholars have conducted studies on beam domain implementation in [23]-[28], including mmWave beam alignment, mmWave power leakage, beam non-orthogonal multiple access (NOMA), beam focusing, and mmWave beam synchronization. However, they have certain limitations without considering the scattering environment. Meanwhile, the channel non-stationarity is not fully considered in papers on conventional BDCM [16]-[18].

TABLE I
Key parameters

key parameter	
$A_{i,j}$	Antenna in the jth row and the ith column of the UPA
P_h,P_v	Dimensions of the array in azimuth and elevation,respectively
P_k	power of the kth path
d_h,d_v	Spacings of adjacent antennas in azimuth and elevation,respectively
v, α	Speed and travel azimuth angle of the UT,respectively
D	Distance between the center of Tx and Rx
$\theta^T_{p,k}, \theta^R_{q,k}$	Azimuth angles of kth path at the BS and UT sides,respectively
$\varphi^T_{p,k}, \varphi^R_{q,k}$	Elevation angles of kth path at the BS and UT sides,respectively
$D^T_{m/s}, D^R_{n/s}$	Distance between the cluster and Tx/Rx
$\alpha^T_{m/s}, \alpha^R_{n/s}$	Azimuth angles of cluster at Tx and Rx
$\beta^T_{m/s}, \beta^R_{n/s}$	Elevation angles of cluster at Tx and Rx

Taking both scattering environment and non-stationarity into consideration, recent works on BDCM can be summarized into two types: single-bouncing models and double-bouncing models.

A. Single-bouncing models

The model in [19] is developed by extending the GBSM ellipse model with single-bouncing birth-death process. The near-field effect and spatial-temporal non-stationarity are considered in BDCM for the first time. The proposed model maintains the same cluster-level performance as the existing GBSM with significantly reduced computational complexity. However, extensive channel measurements suggest that there are simultaneously single-bouncing and double-bouncing rays in the different propagation scenarios, which cannot be precisely described by these models [21].

B. Double-bouncing models

The cluster VR concept [29] is introduced into the beam domain model in [20] with double-bouncing cluster process. VR refers to an area over the antenna array. Only the antennas in the assigned VR can observe the corresponding clusters. The model in [30] is proposed to meet the on-demand communications in unmanned aerial vehicles (UAVs) scenarios. The accuracy, complexity, and pervasiveness of the model are also analyzed. Unfortunately, the models above neglect the correlation between AoAs and AoDs of single-bouncing clusters. The double-bouncing models cannot represent the single-bouncing rays even if ignoring the virtual link [31].

III. BDCM for Massive MIMO Communications at mmWave Bands

The massive MIMO communication system at mmWave band is depicted in Fig. 1. The transmitter (Tx) employs a fixed large uniform plane antenna array (UPA) and is aligned on Y-Z planes with dimensions $P_h \times P_v$. The single-antenna receiver (Rx) represents the user terminal (UT) which can move in an arbitrary direction α and an arbitrary speed v.

In the propagation environments, the multipath components (MPCs) are typically distributed as clusters, sharing similar delays and angles. Considering the rich scattering environment at the mmWave band, clusters are defined in two types: 1) SBCs (single-bouncing clusters), the square pattern in Fig. 1; 2) DBCs (double-bouncing clusters), the triangle pattern in Fig. 1. Related parameters and definitions are listed in Table I.

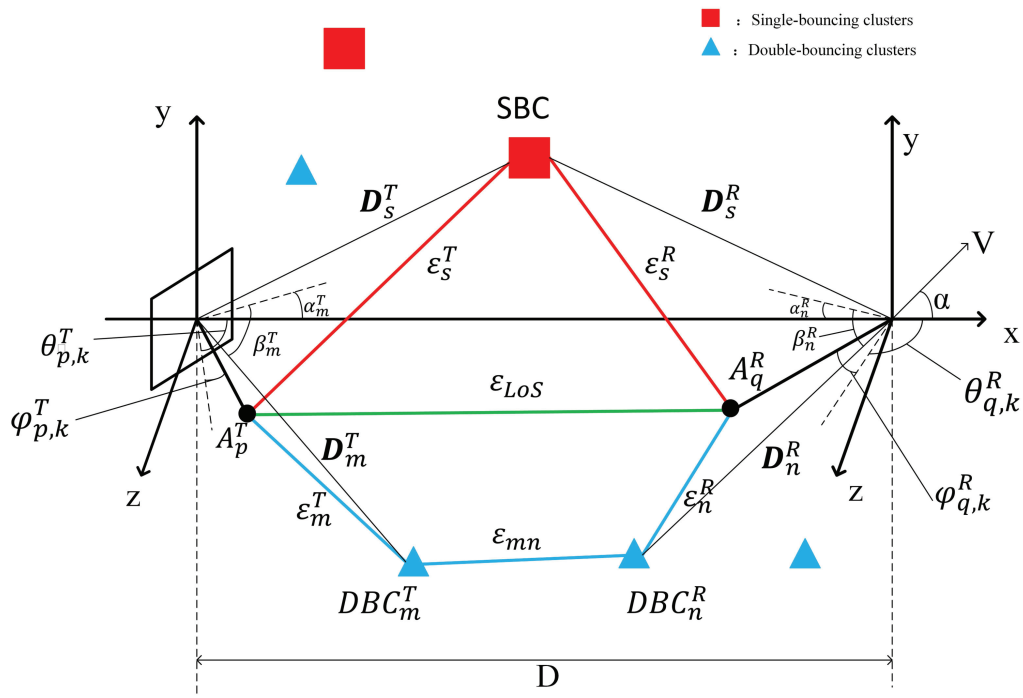

Fig. 1. mmWave massive MIMO communication system with angular parameters and single- and double-bouncing scattering propagation.

A. GBSM with mixed-bouncing clusters

In the model, each of rays is assumed to be uncorrelated and the power assigned to each ray is individually calculated [32]. Specifically, the proposed model does not assume far field conditions for conventional MIMO channels and the wavefront of each link is spherical [33], [34]. Considered the mixed LoS ray, the single-bouncing ray, and the double-bouncing ray, the channel impulse response (CIR) between the jth (j = 1, ..., P_v) column and the ith (i = 1, ..., P_h) row antenna of the UPA and UTs is given as

$$h_{ij,k}(\tau)= h_{ij,k}^{LoS}(\tau) + h_{ij,k}^{SBC}(\tau) + h_{ij,k}^{DBC}(\tau) \tag{1}$$

where

$$h_{ij,k}^{LoS}(\tau)= \frac{1}{\sqrt{P_h \times P_v}}\sqrt{\frac{K_R}{K_R+1}} * f_{i,j}^{G}(\tau) \cdot e^{j\left(2\pi f^{LoS}\tau+\phi^{LoS}\right)} \tag{2}$$

$$h_{ij,k}^{SBC}(\tau)= \frac{1}{\sqrt{P_h \times P_v}}\sqrt{\frac{\eta_S P_k}{K_R+1}} * f_{i,j}^{G}(\tau) \cdot \lim_{S\to\infty}\sum_{s=1}^{S}\frac{e^{j\left(2\pi f^{SBC}\tau+\phi^{SBC}\right)}}{\sqrt{S}} \tag{3}$$

$$h_{ij,k}^{DBC}(\tau)= \frac{1}{\sqrt{P_h \times P_v}}\sqrt{\frac{\eta_D P_k}{K_R+1}} * f_{i,j}^{G}(\tau) \cdot \lim_{M,N\to\infty}\sum_{m,n=1}^{M,N}\frac{e^{j\left(2\pi f^{DBC}\tau+\phi^{DBC}\right)}}{\sqrt{MN}} \tag{4}$$

where the symbol K_R is the Rice factor, denoting the power contribution of the LoS rays and the NLoS rays, P_k is the normalized total power between Tx and Rx of the kth mix-bouncing ray, η_S and η_D are the power contribution ratio of SBCs and DBCs, respectively, satisfying η_S+η_D =1, the symbols f and ϕ are Doppler frequency and phase, respectively, and $f_{i,j}^{G}(\tau)$ is the transfer function between UPA and UTs based on GBSM as follows [20]

$$f_{ij,k}^{G}(\tau) = e^{j2\pi[v_k\tau - f_c\tau_k + \Phi_k]} \times e^{j\frac{2\pi}{\lambda}\left[(i-1)d_h\cos\varphi_{p,k}^{T}\sin\theta_{p,k}^{T}+(j-1)d_v\sin\varphi_{p,k}^{T}\right]} \tag{5}$$

where the first half of the expression represents the frequency and phase shifts caused by the movement of UTs. The doppler frequency is expressed as $v_k = f_k \cdot \cos\varphi_{q,k}^{R} \cdot \cos(\theta_{q,k}^{R} - \alpha)$, where $f_k = v/\lambda$,and λ accounts for the wavelength. Furthermore, f_c and τ_k are the carrier frequency and the path delay of the kth ray, respectively. The phase shift Φ_k of the kth ray is uniformly distributed in $[0, 2\pi)$, i.e., $\Phi_k \sim U[0, 2\pi)$. The second half of the expression is the response of the UPA side in antenna domain.

B. VR model of the single-bouncing and double-bouncing clusters

In the proposed model, a VR is defined as the projection of the influence region caused by the clusters in the array domain. The length and position of the VR in the horizontal and vertical directions for the kth path in the UPA are defined as

$$\mathcal{L}_{\mathrm{k}}^{\mathrm{h/v}} = \left(\mathrm{I}_{\mathrm{e,k}}^{\mathrm{h/v}} - \mathrm{I}_{\mathrm{s,k}}^{\mathrm{h/v}}\right) \cdot \mathrm{d}_{\mathrm{h/v}} \tag{6}$$

$$O(\tau) = \left(\frac{\left(\mathrm{I}_{\mathrm{e,k}}^{\mathrm{h}} - \mathrm{I}_{\mathrm{s,k}}^{\mathrm{h}}\right)}{2}, \frac{\left(\mathrm{I}_{\mathrm{e,k}}^{\mathrm{v}} - \mathrm{I}_{\mathrm{s,k}}^{\mathrm{v}}\right)}{2}\right) \tag{7}$$

where $\mathrm{I}^{\mathrm{h}}_{\mathrm{e,k}}$ and $\mathrm{I}^{\mathrm{h}}_{\mathrm{s,k}}$ are the end and start column indexes of the UPA, respectively. $\mathrm{I}^{\mathrm{v}}_{\mathrm{e,k}}$ and $\mathrm{I}^{\mathrm{v}}_{\mathrm{s,k}}$ are the respective end and start row indexes of the UPA, which follow a uniform distribution [36], i.e., $\mathrm{I}^{\mathrm{h}}_{\mathrm{e,k}}$, $\mathrm{I}^{\mathrm{h}}_{\mathrm{s,k}} \sim U(0, P_h)$ and $\mathrm{I}^{\mathrm{v}}_{\mathrm{e,k}}$, $\mathrm{I}^{\mathrm{v}}_{\mathrm{s,k}} \sim U(0, P_v)$.

In addtional, the cluster movement also has a great influence on VR as shown in Fig. 2. When a SBC is moved, both the TX and Rx are effected and lead to a shift in the length and position of the VR; while due to virtual links, the movement of a DBC often exists only at one end. Therefore, considering the case of SBC movement, the VR should be updated at different moments to simulate the real propagation conditions, i.e.,

$$O(\tau_2) = O(\tau_1) + \Delta \boldsymbol{d}. \tag{8}$$

where $\Delta \boldsymbol{d}$ is the projection length vector of the moving SBC on the antenna array.

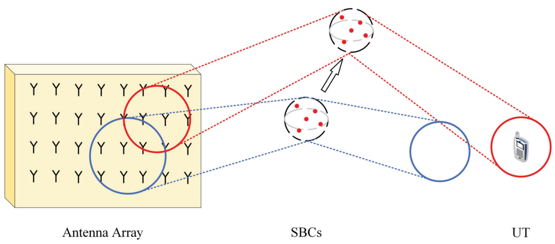

(a)

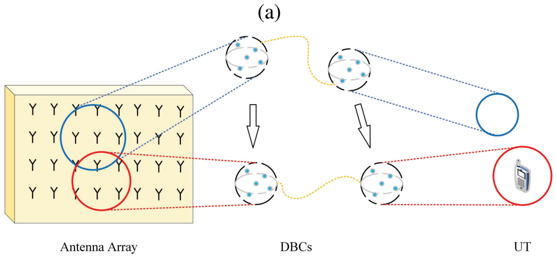

(b)

Fig. 2. Examples of influence of clusters movement on the VR (a) SBCs, and (b) DBCs.

Specifically, it should be noted that the clusters' VR lengths are different in both the horizontal and vertical directions in the UPA due to the non-stationary behavior of the isotropic channel in the array domain. In our simulation, the gain of VR is configured to be either 1 or 0, representing the activity or not of the relevant cluster, and the parameter ε is the proportion of SBCs in VR. It is worth mentioning that larger ε means a sparser scattering environment.

C. Model for each ray

As shown in Fig. 1, a lot of SBCs and DBCs are distributed in the scattering environment. The distance between the cluster and Tx/Rx follows an exponential distribution [35]: $D^T_{m/s}(t), D^R_{n/s}(t) = k_{dd/ds} e^{-k_{dd/ds}}$, where k_{dd} and k_{ds} are the distance parameters for DBCs and SBCs, respectively. Distance vectors between the clusters and Tx and Rx are denoted as $D^T_{m/s}(t)$ and $D^R_{n/s}(t)$, respectively, which can be given as follows

$$\boldsymbol{D}^T_{m/s}(t) = D^T_{m/s}(t) \begin{bmatrix} \cos \alpha^T_{m/s}(t) \cos \beta^T_{m/s}(t) \\ \sin \alpha^T_{m/s}(t) \cos \beta^T_{m/s}(t) \\ \sin \beta^T_{m/s}(t) \end{bmatrix} \tag{9}$$

and

$$\boldsymbol{D}^R_{n/s}(t) = D^R_{n/s}(t) \begin{bmatrix} \cos \alpha^R_{n/s}(t) \cos \beta^R_{n/s}(t) \\ \sin \alpha^R_{n/s}(t) \cos \beta^R_{n/s}(t) \\ \sin \beta^R_{n/s}(t) \end{bmatrix} + \boldsymbol{D} \tag{10}$$

where $D^T_{m/s}(t)$ and $D^R_{n/s}(t)$ are the Frobenius norms of $\boldsymbol{D}^T_{m/s}(t)$ and $\boldsymbol{D}^R_{n/s}(t)$, respectively, and $\boldsymbol{D}$ is the initial position vector of the receiver and is assumed to equal $[D, 0, 0]^T$.

1) LoS components: The LoS distance vector $\varepsilon^{LoS}_{ij}(t)$ is calculated according to the geometrical relationship in Fig. 1 as follows

$$\varepsilon^{LoS}_{ij}(t) = \left\| \boldsymbol{D}^{LoS}_{ij}(t) \right\| = \left\| \boldsymbol{A}^R(t) - \boldsymbol{A}^T_{ij}(t) \right\| \tag{11}$$

where $\boldsymbol{A}^R(t)$ and $\boldsymbol{A}^T_{ij}(t)$ represent the position vectors of receive antenna $Ant^R(t)$ and (i, j)th transmit antenna $Ant^T_{ij}(t)$, respectively. Then, the doppler frequency and phase shift can be calculated as follows

$$f^{LoS}_{ij}(t) = \frac{f^T_{\max} < \boldsymbol{D}^{LoS}_{ij}(t), \boldsymbol{v}_T >}{\left\| \boldsymbol{D}^{LoS}_{ij}(t) \right\| \left\| \boldsymbol{v}_T \right\|} + \frac{f^R_{\max} < \boldsymbol{D}^{LoS}_{ij}(t), \boldsymbol{v}_R >}{\left\| \boldsymbol{D}^{LoS}_{ij}(t) \right\| \left\| \boldsymbol{v}_R \right\|} \tag{12}$$

and

$$\phi^{LoS}_{ij}(t) = \phi_0 + \frac{2\pi}{\lambda} \varepsilon^{\mathrm{LoS}}_{ij}(t) = \phi_0 + \frac{2\pi}{\lambda} \left\| \boldsymbol{D}^{LoS}_{ij}(t) \right\| \tag{13}$$

where f^T_{max} and f^R_{max} are the respective maximum doppler frequencies at transmit and receive antennas, v_T and v_R are the velocity vectors of the Tx and Rx, respectively, ϕ_0 is the initial phase, and the operator $< \cdot >$ represents the inner product.

2) SBC components: For the single-bouncing ray, the complex channel gain between the antennas A^T_{ij} and A^R through the kth ray within cluster C_s can be expressed as

- if $A^T_{ij} \in A^T_{C_s}(t)$ and $A^R \in A^R_{C_s}(t)$, and $\boldsymbol{D} \geq \boldsymbol{D}_T$, the complex channel gain h^s_{ij,k,C_s} is an effective link caused by the kth single-bouncing ray within cluster C_s
- otherwise

$$h^s_{ij,k,C_s} = 0 \tag{14}$$

The distance vector of the single-bouncing link is calculated as follows

$$\begin{aligned} \varepsilon^{SBC}_{ij,s}(t) =& \varepsilon^T_s(t) + \varepsilon^R_s(t) \\ =& \left\| \boldsymbol{D}^T_s(t) - \boldsymbol{A}^T_{\boldsymbol{ij}}(t) \right\| + \left\| \boldsymbol{D}^R_s(t) - \boldsymbol{A}^R(t) \right\|. \end{aligned} \tag{15}$$

It should be noticed that, the transmission distance between the SBCs and Tx/Rx, i.e., $\boldsymbol{D}^T_s(t)$ and $\boldsymbol{D}^R_s(t)$, are naturally correlated. In other words, the transmission distance between SBCs and Rx, $\boldsymbol{D}^R_s(t)$ should be calculated as $\boldsymbol{D}^R_s(t) = \boldsymbol{D}^{LoS}_{ij}(t) - \boldsymbol{D}^T_s(t)$.

Then, the doppler frequency and phase shift can be respectively calculated as follows

$$\begin{aligned} f^{SBC}_{ij,s}(t) =& \frac{f^T_{\max} < \boldsymbol{D}^T_s(t) - \boldsymbol{A}^T_{ij}(t), \boldsymbol{v}_T >}{\left\| \boldsymbol{D}^T_s(t) - \boldsymbol{A}^T_{\boldsymbol{p}}(t) \right\| \left\| \boldsymbol{v}_T \right\|} \\ &+ \frac{f^R_{\max} < \boldsymbol{D}^R_s(t) - \boldsymbol{A}^R(t), \boldsymbol{v}_R >}{\left\| \boldsymbol{D}^R_s(t) - \boldsymbol{A}^R_{\boldsymbol{q}}(t) \right\| \left\| \boldsymbol{v}_R \right\|} \end{aligned} \tag{16}$$

and

$$\begin{aligned}\phi_{ij,s}^{SBC}(t) &= \phi_0 + \frac{2\pi}{\lambda}\varepsilon_{ij,s}^{SBC}(t)\\ &= \phi_0 + \frac{2\pi}{\lambda}\left(\left\|\boldsymbol{D}_s^T(t)-\boldsymbol{A}_{ij}^T(t)\right\|+\left\|\boldsymbol{D}_s^R(t)-\boldsymbol{A}^R(t)\right\|\right).\end{aligned} \tag{17}$$

3) DBC components: Similarly, for the double-bouncing ray, the complex channel gain between the antennas A_{ij}^T and A^R through the kth ray within cluster C_d can be expressed as

- if $A_{ij}^T \in A_{C_d}^T(t)$ and $A^R \in A_{C_d}^R(t)$, the complex channel gain h_{ij,k,C_d}^s is an effective link caused by the kth double-bouncing ray within cluster C_d
- otherwise

$$h_{ij,k,C_d}^d = 0 \tag{18}$$

The distance vector of the double-bouncing link is calculated as follows

$$\begin{aligned}\varepsilon_{ij,n,m}^{DBC}(t) &= \varepsilon_m^T(t)+\varepsilon_n^R(t)+\varepsilon_{mn}(t)\\ &= \left\|\boldsymbol{D}_m^T(t)-\boldsymbol{A}_{\boldsymbol{ij}}^T(t)\right\|+\left\|\boldsymbol{D}_n^R(t)-\boldsymbol{A}^R(t)\right\|+c\tilde{\tau}_k(t)\end{aligned} \tag{19}$$

where $\tilde{\tau}_k(t)$ is the abstracted delay of the virtual link between the first- and last-bouncing clusters in the scattering environment which follows as in the WINNER II channel model [34]

$$\tilde{\tau}_k = -r_\tau \sigma_\tau \cdot ln u_n \tag{20}$$

where u_n is uniformly distributed within (0,1), r_τ is the delay scalar and σ_τ is a randomly generated delay spread (alternative parameters for different scenarios can be found in [33]).

In additional, the first bouncing and the last bouncing rays are independent of each other and randomly generated which is distinct from the generation of SBCs. Note that $\boldsymbol{D}_m^T(t)$ and $\boldsymbol{D}_n^R(t)$ are indepentdent of each other.

Then, the doppler frequency and phase shift can be respectively calculated as follows

$$\begin{aligned}f_{pq,n,m}^{DBC}(t) &= \frac{f_{\max}^T < \left\|\boldsymbol{D}_m^T(t)-\boldsymbol{A}_{\boldsymbol{p}}^T(t)\right\|, \boldsymbol{v}_T >}{\left\|\boldsymbol{D}_m^T(t)-\boldsymbol{A}_{\boldsymbol{p}}^T(t)\right\|\left\|\boldsymbol{v}_T\right\|}\\ &+ \frac{f_{\max}^R < \boldsymbol{D}_n^R(t)-\boldsymbol{A}_{\boldsymbol{q}}^R(t), \boldsymbol{v}_R >}{\left\|\boldsymbol{D}_n^R(t)-\boldsymbol{A}_{\boldsymbol{q}}^R(t)\right\|\left\|\boldsymbol{v}_R\right\|}\end{aligned} \tag{21}$$

and

$$\phi_{pq,n,m}^{DBC}(t) = \phi_0 + \frac{2\pi}{\lambda}\varepsilon_{pq,n,m}^{DBC}(t). \tag{22}$$

The mean power for kth path is generated as [34]

$$P_k = \exp\left(-\tilde{\tau}_k \frac{r_\tau - 1}{r_\tau \sigma_\tau}\right) 10^{-\frac{z_n}{10}} \tag{23}$$

where Z_n follows a Gaussian distribution $N \sim (0, \nu_\tau)$,ν_τ being a shadow fading standard deviation for different scenarios. The power for the kth path is then normalized into $\tilde{P}_k = \frac{P_k}{\sum_K P_k}$.

In our simulation, the mean power for SBCs are relatively larger than DBCs while numbers of SBCs are less than DBCs to describe the real scattering environment. The mixed-bouncing clusters generation algorithm is summarized as follows.

Algorithm 1: Mixed-bouncing Clusters Generation

Input: numbers of SBCs, N_S, and DBCs, N_D in the scenario;
Output: $\boldsymbol{D}_s^T(t)$; $\boldsymbol{D}_m^T(t)$; $\boldsymbol{D}_n^R(t)$;
Initialization: set the values of transceiver distance $\boldsymbol{D}$;
for $n = 1, \cdots, N_S$ **do**
  if $A_{ij}^T \in A_{C_s}^T(t)$, $A^R \in A_{C_s}^R(t)$ **then**
    Generate vectors of SBCs $\boldsymbol{D}_s^T(t)$;
  else
    $h_{ij,k,C_s}^s = 0$;
  end
end
for $n = 1, \cdots, N_D$ **do**
  if $A_{ij}^T \in A_{C_d}^T(t)$ *and* $A^R \in A_{C_d}^R(t)$ **then**
    Generate vectors of DBCs $\boldsymbol{D}_m^T(t)$ and $\boldsymbol{D}_n^R(t)$, separately;
  else
    $h_{ij,k,C_d}^d = 0$;
  end
end

D. Novel BDCM with mixed-bouncing clusters

To simplify the analysis, let $\theta_k^{az} = \frac{d_h}{\lambda}\cos\varphi_{p,k}^T \sin\theta_{p,k}^T$, $\theta_k^{el} = \frac{d_v}{\lambda}\sin\varphi_{p,k}^T$. Therefore, the response matrix for UPA side can be rewritten as

$$\begin{aligned}\boldsymbol{U}\left(\theta_k^{az}, \theta_k^{el}\right) &= \begin{bmatrix} 1 & \cdots & e^{j2\pi(P_h-1)\theta_k^{az}} \\ e^{j2\pi\theta_k^{el}} & \cdots & e^{j2\pi\left[\theta_k^{el}+(P_h-1)\theta_k^{az}\right]} \\ \vdots & \ddots & \vdots \\ e^{j2\pi(P_v-1)\theta_k^{el}} & \cdots & e^{j2\pi\left[(P_v-1)\theta_k^{el}+(P_h-1)\theta_k^{az}\right]} \end{bmatrix}\\ &= \boldsymbol{b}\left(\theta_k^{el}\right) \otimes \boldsymbol{a}\left(\theta_k^{az}\right)\end{aligned} \tag{24}$$

where $\boldsymbol{a}\left(\theta_k^{az}\right)$ and $\boldsymbol{b}\left(\theta_k^{el}\right)$ are the response vectors in azimuth and elevation, respectively, i.e.,

$$\boldsymbol{a}\left(\theta_k^{az}\right) = \left[1, e^{j2\pi\theta_k^{az}}, \ldots, e^{j2\pi(P_h-1)\theta_k^{az}}\right] \tag{25}$$

and

$$\boldsymbol{b}\left(\theta_k^{el}\right) = \left[1, e^{j2\pi\theta_k^{el}}, \ldots, e^{j2\pi(P_v-1)\theta_k^{el}}\right]. \tag{26}$$

The beam domain is transferred based on GBSM through a unitary matrix-based beamforming operation as follows [15]

$$\boldsymbol{U}_B(t) = \boldsymbol{U}\left(\theta_k^{az}, \theta_k^{el}\right) \cdot \widetilde{\boldsymbol{U}}^* \tag{27}$$

where $\widetilde{\boldsymbol{U}}$ is the beamforming matrix as

$$\widetilde{\boldsymbol{U}} = \widetilde{\boldsymbol{U}}_{el} \otimes \widetilde{\boldsymbol{U}}_{az} \tag{28}$$

with

$$\widetilde{\boldsymbol{U}}_{az} = \frac{1}{\sqrt{P_h}}\boldsymbol{a}\left(\tilde{\theta}_i^{az}\right), \widetilde{\boldsymbol{U}}_{el} = \frac{1}{\sqrt{P_v}}\boldsymbol{b}\left(\tilde{\theta}_j^{el}\right). \tag{29}$$

The response sample vectors $\widetilde{\boldsymbol{U}}_{az}$ and $\widetilde{\boldsymbol{U}}_{el}$ are the uniformly spaced spatial frequencies associated with P_h and P_v, respectively, i.e., $\tilde{\theta}_i^{az} = \frac{2i-1}{2P_h} - 0.5, i = 1, \ldots, P_h$ and $\tilde{\theta}_j^{el} = \frac{2j-1}{2P_v} - 0.5, j = 1, \ldots, P_v$.

Considered the VR effect, the antenna domain channel matrix $\boldsymbol{U(t)}$ at UPA side can be transformed into beam domain channel matrix $\boldsymbol{U_B(t)}$.

$$\begin{aligned}\boldsymbol{U}_B(t) &= \boldsymbol{U}\left(\theta_k^{az}, \theta_k^{el}\right) \cdot \widetilde{\boldsymbol{U}}^* \\ &= \left(\boldsymbol{b}\left(\theta_k^{el}\right) \otimes \boldsymbol{a}\left(\theta_k^{az}\right)\right) \cdot \left(\boldsymbol{b}\left(\tilde{\theta}_j^{el}\right)^* \otimes \boldsymbol{a}\left(\tilde{\theta}_i^{az}\right)^*\right) \\ &= \left(\boldsymbol{b}\left(\theta_k^{el}\right) \cdot \boldsymbol{b}\left(\tilde{\theta}_j^{el}\right)^*\right) \otimes \left(\boldsymbol{a}\left(\theta_k^{az}\right) \cdot \boldsymbol{a}\left(\tilde{\theta}_i^{az}\right)^*\right) \\ &= \frac{1}{\sqrt{P_v}} \sum_{a=I_s^v}^{I_e^v} e^{j2\pi b\left(\theta_k^{el} - \widetilde{\theta}_j^{el}\right)} \cdot \frac{1}{\sqrt{P_h}} \sum_{b=I_s^h}^{I_e^h} e^{j2\pi a\left(\theta_k^{az} - \widetilde{\theta}_i^{az}\right)} \\ &= \frac{1}{\sqrt{P_v \times P_h}} \cdot f_{I_s^h, I_e^h}\left(\theta_k^{az} - \tilde{\theta}_i^{az}\right) \cdot f_{I_s^v, I_e^v}\left(\theta_k^{el} - \tilde{\theta}_j^{el}\right)\end{aligned} \tag{30}$$

where

$$f_{I_s, I_e}(x) = e^{j\pi x(I_e + I_s - 2)} \frac{\sin\left[\pi x\left(I_e - I_s + 1\right)\right]}{\sin(\pi x)}. \tag{31}$$

where the symbols I_s and I_e are the start and end indexes in the UPA of the cluster VR, respectively.

Finally, the complete beam domain channel matrix $\boldsymbol{H}_{ij,k}^B(t)$ considering mixed-bouncing ray is obtained as shown at the top of next page.

IV. Statistical properties of the beam domain channel

A. Spatial-temporal correlation function

The spatial-temporal correlation function (ST-CF) between channel element $h_{ij,k}(t)$ and $h_{i'j',k}(t+\Delta t)$ is defined as [38]

$$\rho_{ij,i'j'(\delta_t,\delta_r,\Delta t;t)} = E\left[\frac{h_{ij}^*(t) h_{i'j'}(t+\Delta t)}{\left|h_{ij}^*(t)\right| \cdot \left|h_{i'j'}(t+\Delta t)\right|}\right] \tag{33}$$

where δ_t and δ_r are the antenna spacings at Tx and Rx, respectively. Based on the uncorrelated scattering assumption, (33) can be rewritten as the sum of the LoS, SBC, and DBC components

$$\begin{aligned}\rho_{ij,i'j'(\delta_t,\delta_r,\Delta t;t)} = &\rho_{ij,i'j'(\delta_t,\delta_r,\Delta t;t)}^{LoS} \\ &+ \rho_{ij,i'j'(\delta_t,\delta_r,\Delta t;t)}^{SBC} \\ &+ \rho_{ij,i'j'(\delta_t,\delta_r,\Delta t;t)}^{DBC}.\end{aligned} \tag{34}$$

By substituting (32) into (34),ST-CF is expressed as

$$\begin{aligned}&\rho_{ij,i'j'(\delta_T,\delta_R,\Delta t;t)} \\ &= \sum_{k=1}^{K} e^{-j2\pi v_k \Delta t} \cdot e^{j\pi \frac{\left(I_s^h + I_e^h - 2\right)\Delta i}{P_h}} e^{j\pi \frac{\left(I_S^v + I_e^v - 2\right)\Delta j}{P_v}} \\ &\cdot \left(\begin{aligned}&\tfrac{K_R}{K_R+1} \cdot e^{j\Phi^{LOS}} \\ &+ \tfrac{\eta_S P_k}{K_R+1} \cdot \mathbb{E}\Big[\lim_{S\to\infty} \textstyle\sum_{s=1}^{S} \frac{e^{j\Phi^{SBC}}}{S}\Big] \\ &+ \tfrac{\eta_D P_k}{K_R+1} \cdot \mathbb{E}\Big[\lim_{M,N\to\infty} \textstyle\sum_{m,n=1}^{M,N} \frac{e^{j\Phi^{DBC}}}{MN}\Big]\end{aligned}\right) \\ &\cdot D_{I_e^v - I_S^v + 1}\left(\theta_k^{el} - \tilde{\theta}_j^{el}\right) \cdot D_{I_e^v - I_s^v + 1}\left(\theta_k^{el} - \tilde{\theta}_{j'}^{el}\right) \\ &\cdot D_{I_e^h - I_s^h + 1}\left(\theta_k^{az} - \tilde{\theta}_i^{az}\right) \cdot D_{I_e^h - I_s^h + 1}\left(\theta_k^{az} - \tilde{\theta}_{i'}^{az}\right)\end{aligned} \tag{35}$$

where $\Delta i = i' - i$, $\Delta j = j' - j$, $D_n(x) = \frac{sin(\pi n x)}{sin(\pi x)}$ is the Dirichlet sinc function of degree n, and

$$\begin{aligned}\Phi^{LoS} &= 2\pi f_{i'j'}^{LoS}(t+\Delta t)(t+\Delta t) - 2\pi f_{ij}^{LoS}(t)t \\ &\quad + \phi_{i'j'}^{LoS}(t+\Delta t) - \phi_{ij}^{LoS}(t)\end{aligned} \tag{36}$$

$$\begin{aligned}\Phi^{SBC} &= 2\pi f_{i'j'}^{SBC}(t+\Delta t)(t+\Delta t) - 2\pi f_{ij}^{SBC}(t)t \\ &\quad + \phi_{i'j'}^{SBC}(t+\Delta t) - \phi_{ij}^{SBC}(t)\end{aligned} \tag{37}$$

$$\begin{aligned}\Phi^{DBC} &= 2\pi f_{i'j'}^{DBC}(t+\Delta t)(t+\Delta t) - 2\pi f_{ij}^{DBC}(t)t \\ &\quad + \phi_{i'j'}^{DBC}(t+\Delta t) - \phi_{ij}^{DBC}(t).\end{aligned} \tag{38}$$

1) Spatial cross-correlation function: Setting $\Delta t = 0$ and Δi, Δj as variables, the ST-CF reduces to the spatial cross-correlation function (CCF).

$$\begin{aligned}&\rho_{ij,i'j'(\delta_t,\delta_r;t)} \\ &= \sum_{k=1}^{K} e^{j\pi \frac{\left(I_s^h + I_e^h - 2\right)\Delta i}{P_h}} e^{j\pi \frac{\left(I_S^v + I_e^v - 2\right)\Delta j}{P_v}} \\ &\cdot \left(\begin{aligned}&\tfrac{K_R}{K_R+1} \cdot e^{j\Phi^{LOS}(\delta_t,\delta_r;t)} \\ &+ \tfrac{\eta_S P_k}{K_R+1} \cdot \mathbb{E}\Big[\lim_{S\to\infty} \textstyle\sum_{s=1}^{S} \frac{e^{j\Phi^{SBC}(\delta_t,\delta_r;t)}}{S}\Big] \\ &+ \tfrac{\eta_D P_k}{K_R+1} \cdot \mathbb{E}\Big[\lim_{M,N\to\infty} \textstyle\sum_{m,n=1}^{M,N} \frac{e^{j\Phi^{DBC}(\delta_t,\delta_r;t)}}{MN}\Big]\end{aligned}\right) \\ &\cdot D_{I_e^v - I_S^v + 1}\left(\theta_k^{el} - \tilde{\theta}_j^{el}\right) \cdot D_{I_e^v - I_s^v + 1}\left(\theta_k^{el} - \tilde{\theta}_{j'}^{el}\right) \\ &\cdot D_{I_e^h - I_s^h + 1}\left(\theta_k^{az} - \tilde{\theta}_i^{az}\right) \cdot D_{I_e^h - I_s^h + 1}\left(\theta_k^{az} - \tilde{\theta}_{i'}^{az}\right)\end{aligned} \tag{39}$$

where

$$\begin{aligned}\Phi^{LoS}\left(\delta_t, \delta_r; t\right) &= 2\pi f_{i'j'}^{LoS}(t)t - 2\pi f_{ij}^{LoS}(t)t \\ &\quad + \phi_{i'j'}^{LoS}(t) - \phi_{ij}^{LoS}(t)\end{aligned} \tag{40}$$

$$\begin{aligned}\Phi^{SBC}\left(\delta_t, \delta_r; t\right) &= 2\pi f_{i'j'}^{SBC}(t)t - 2\pi f_{ij}^{SBC}(t)t \\ &\quad + \phi_{i'j'}^{SBC}(t) - \phi_{ij}^{SBC}(t)\end{aligned} \tag{41}$$

$$\begin{aligned}\Phi^{DBC}\left(\delta_t, \delta_r; t\right) &= 2\pi f_{i'j'}^{DBC}(t)t - 2\pi f_{ij}^{DBC}(t)t \\ &\quad + \phi_{i'j'}^{DBC}(t) - \phi_{ij}^{DBC}(t).\end{aligned} \tag{42}$$

As the spatial CCF $\rho_{ij,i'j'(\delta_T,\delta_R;t)}$ depends the values of i, j, i', and j', the wide-sense stationary (WSS) assumption in the array domain is not valid.

2) Temporal autocorrelation function: By setting $i = i'$, $j = j'$, and δ_t, δ_r fixed at $\lambda/2$, the temporal autocorrelation function (ACF) $\rho_{ij,k(\Delta t;t)}$ is obtained.

$$\begin{aligned}&\rho_{ij(\Delta t;t)} \\ &= \sum_{k=1}^{K} e^{-j2\pi v_k \Delta t} \\ &\cdot \left(\begin{aligned}&\tfrac{K_R}{K_R+1} \cdot e^{j\Phi^{LOS}(\Delta t;t)} \\ &+ \tfrac{\eta_S P_k}{K_R+1} \cdot \mathbb{E}\Big[\lim_{S\to\infty} \textstyle\sum_{s=1}^{S} \frac{e^{j\Phi^{SBC}(\Delta t;t)}}{S}\Big] \\ &+ \tfrac{\eta_D P_k}{K_R+1} \cdot \mathbb{E}\Big[\lim_{M,N\to\infty} \textstyle\sum_{m,n=1}^{M,N} \frac{e^{j\Phi^{DBC}(\Delta t;t)}}{MN}\Big]\end{aligned}\right) \\ &\cdot \mathrm{D}_{I_e^v - I_s^v + 1}^2\left(\theta_k^{el} - \tilde{\theta}_j^{el}\right) \mathrm{D}_{I_e^h - I_s^h + 1}^2\left(\theta_k^{az} - \tilde{\theta}_i^{az}\right)\end{aligned} \tag{43}$$

where

$$\begin{aligned}\Phi^{LoS}(\Delta t; t) &= 2\pi f_{ij}^{LoS}(t+\Delta t)(t+\Delta t) - 2\pi f_{ij}^{LoS}(t)t \\ &\quad + \phi_{ij}^{LoS}(t+\Delta t) - \phi_{ij}^{LoS}(t)\end{aligned} \tag{44}$$

$$\boldsymbol{H}_{ij,k}^{B}(t) = \frac{1}{\sqrt{P_h \times P_v}} \sum_{k=1}^{K} e^{j2\pi[v_k\tau - f_c\tau_k + \Phi_k]} \times f_{I_s^h, I_e^h}\left(\theta_k^{az} - \tilde{\theta}_i^{az}\right) \cdot f_{I_s^v, I_e^v}\left(\theta_k^{el} - \tilde{\theta}_j^{el}\right) \cdot\left(\sqrt{\frac{K_R}{K_R+1}} e^{j\left(2\pi f^{LoS}\tau + \phi^{LoS}\right)} + \sqrt{\frac{\eta_S P_k}{K_R+1}} \lim_{S\to\infty} \sum_{s=1}^{S} \frac{e^{j\left(2\pi f^{SBC}\tau + \phi^{SBC}\right)}}{\sqrt{S}} + \sqrt{\frac{\eta_D P_k}{K_R+1}} \lim_{M,N\to\infty} \sum_{m,n=1}^{M,N} \frac{e^{j\left(2\pi f^{DBC}\tau + \phi^{DBC}\right)}}{\sqrt{MN}}\right) \tag{32}$$

$$\Phi^{SBC}(\Delta t; t) = 2\pi f_{ij}^{SBC}(t+\Delta t)(t+\Delta t) - 2\pi f_{ij}^{SBC}(t)t + \phi_{ij}^{SBC}(t+\Delta t) - \phi_{ij}^{SBC}(t) \tag{45}$$

$$\Phi^{DBC}(\Delta t; t) = 2\pi f_{ij}^{DBC}(t+\Delta t)(t+\Delta t) - 2\pi f_{ij}^{DBC}(t)t + \phi_{ij}^{DBC}(t+\Delta t) - \phi_{ij}^{DBC}(t). \tag{46}$$

The elements from the wholly visible beam domain channels in the same beam are roughly uncorrelated. In contrast, the wide beamwidth causes channel elements in VR to be correlated with one another. This suggests that conventional BDCM, which ignores the effects of non-stationarity, as well as SBCs and DBCs, might underestimate the correlation of the channel elements.

B. RMS beam spread

To describe the power dispersion over beam directions, the beam spread is introduced into BDCM. The azimuth beam spread is defined as [20]

$$\sigma_B^{\mathrm{az}} = \sqrt{\frac{\sum_{i,j=1}^{P_h,P_v} |h_{i,j}|^2 \left(\tilde{\phi}_i^{\mathrm{az}} - \mu^{\mathrm{az}}\right)^2}{\sum_{i,j=1}^{P_h,P_v} |h_{i,j}|^2}} \tag{47}$$

where μ^{az} is the mean value of $\tilde{\phi}_i^{\mathrm{az}}$ and is calculated as

$$\mu^{\mathrm{az}} = \frac{\sum_{i,j=1}^{P_h,P_v} |h_{i,j}|^2 \tilde{\phi}_i^{\mathrm{az}}}{\sum_{i,j=1}^{P_h,P_v} |h_{i,j}|^2}. \tag{48}$$

The elevation beam spread σ_B^{el} can be caculated in the same way by replacing $\tilde{\phi}_i^{\mathrm{az}}$ and μ^{az} with $\tilde{\phi}_j^{\mathrm{el}}$ and μ^{el}, respectively.

C. Channel capacity and power leakage

The channel capacity of the proposed model can be calculated as

$$C = log_2(det(I + \frac{\rho}{P_v \times P_h} H_B \cdot H_B^H)) \tag{49}$$

where I represents the identity matrix, and ρ is the signal-to-noise ratio (SNR).

With the large number of antenna arrays, each beam domain channel element corresponds to MPCs associated with a specific physical direction, i.e., $(\theta_k^{az}, \theta_k^{el})$ where multipath fading vanished, and the power leakage can be ignored. However, in actual massive MIMO scenarios, there are typically many MPCs with a short VR length [37] leading to a decrease in spatial resolution and the introduction of multipath fading.

In conventional beam domain channel, the mismatch between physical path angles $(\theta_k^{az}, \theta_k^{el})$ and sampling points $(\tilde{\theta}_i^{az}, \tilde{\theta}_j^{el})$ lead to the power leakage over a range of beam directions [38]. However, current studies ignore the effect of SBCs and DBCs, which makes the channel evaluation results less accurate. The power leakage in the model can be defined as [18]

$$\Gamma = 1 - \frac{\sum_{i\in\Xi\left(\theta_0^{az}, K_h\right), j\in\Xi\left(\theta_0^{el}, K_v\right)} |h_{i,j}|^2}{\sum_{i,j=1}^{P_h,P_v} |h_{i,j}|^2} \tag{50}$$

where $\Xi\left(\theta_0^{az}, K_h\right)$ and $\Xi\left(\theta_0^{el}, K_v\right)$ represent the column and row indexes of the $K_h \times K_v$ subarray centered on the physical direction of MPC, i.e., $(\theta_k^{az}, \theta_k^{el})$, respectively.

V. RESULTS AND ANALYSIS

In this section, the statistical results of the proposed model for beam domain channel are shown. The conventional BDCM (by setting VR cluster proportion ε=0) is compared with the proposed model to show the effect of non-stationarity and SBCs. In the simulations, MPC parameters such as power, delay, and angle are generated according to 3GPP TR38.901 in indoor non-LoS scenarios [35]. The WINNER II model is used to generate some parameters that cannot be estimated from the measurements [34]: the azimuth angles of the cluster follow the von-Mises distribution, where the means and standard deviations are $\mu_s^T = \frac{3\pi}{4}$, $k_s^T = 2$, $\mu_m^T = \pi$, $\mu_n^R = \frac{\pi}{2}$, $k_m^T = 2$, $k_n^R = 2$, and the elevation angles of the cluster follow the cosine distribution with a maximum angle of $\varphi_{max} = \frac{\pi}{12}$. Furthermore, the distance parameters between the SBCs and DBCs to the Tx/Rx is $k_{ds} = 10m$, $k_{dd} = 5m$, respectively [41].

Fig. 3 shows the azimuth and elevation beam spread of the proposed model, respectively. The angular spread and measurement results in [42] are also presented. The measurement was conducted at 11 GHz with a 256-element UPA in a theater scenario [42]. In our simulations, model parameters were optimized by fitting the angular spread to the measured data. μ_{lgASD} and σ_{lgASD} are the mean and standard deviation of the AAoD, and μ_{lgESD} and σ_{lgESD} are the mean and standard deviation of the EAoD in cluster level, respectively [37]. In Fig. 3(a) and (b), for the proposed model with $P_h = 64$, $P_v = 128$, and $\varepsilon = 0$, the beam spread is roughly equal to the angular spread and measurement data. However, with the limited resolution of the array, i.e., $P_h = 16$, $P_v = 64$, and $\varepsilon = 0$, the beam spread is larger due to power leakage. For $P_h = 64$, $P_v = 128$, and $\varepsilon = 0.8$, due to the existence of more VR clusters, the severe power leakage results in significantly larger beam spread. The above results show the correctness of the proposed model.

Fig. 4 shows the normalized spatial CCF between beams for (a) different VR SBCs proportion ε and (b) different

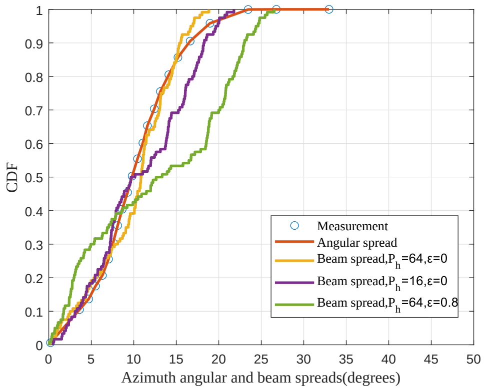

(a)

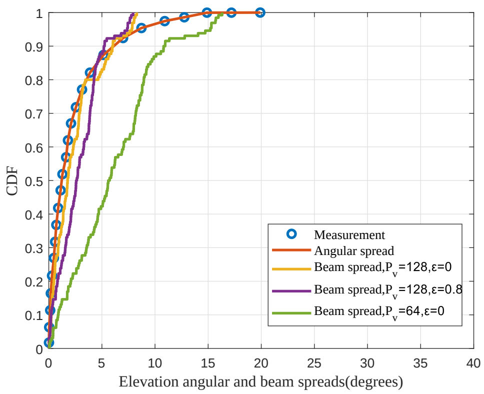

(b)

Fig. 3. Comparison of beam spread, angular spread, and measurement result [42] in (a) azimuth and (b) elevation($\mu_{lgASD} = 1.377°$, $\sigma_{lgASD} = 2.542°$,$\mu_{lgESD} = 0.0103°$, $\sigma_{lgESD} = 0.0351°$).

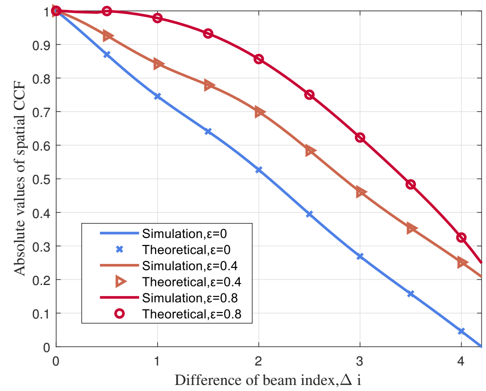

(a)

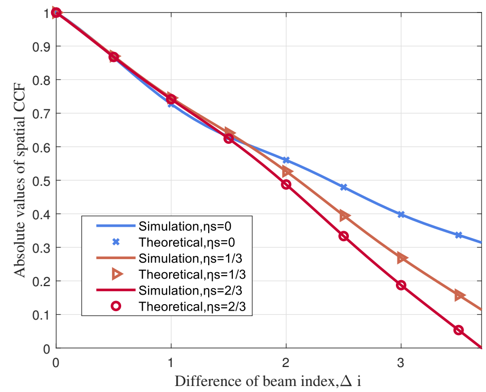

(b)

Fig. 4. CCF for (a) different ε and beam correlation for (b) different η_S ($P_h = P_v = 64$, D=15m, $f_c = 28GHz$, $t = 1s$, $\alpha^T_{m/s} = \beta^T_{n/s} = \frac{\pi}{6}$, $\alpha^R_{m/s} = \beta^R_{n/s} = \frac{\pi}{4}$, $\alpha = \pi/6$, $v = 5m/s$, $\alpha_{sbc} = -\pi/3$, $v_{sbc} = 3m/s$, $\varepsilon = 0.4$, (a) $\eta_S = 1/3$, $\eta_D = 2/3$, (b) $\varepsilon = 0.4$ NLoS).

power contribution η_S. The channel spatial CCF decreases as the beam indexes Δi increases. When the non-stationarity is considered, i.e., the larger ε, the correlation between beams becomes larger. Additionally, the spatial CCF of the proposed model also depends on the power contribution of SBCs and DBCs, i.e., η_S and η_D. When there are only DBCs without SBCs in the scattering environment, the channel exhibits a relatively higher CCF. This indicates that the existing models overestimate the CCF and the proposed model is inherently spatially non-stationary. In addition, as shown in Fig. 4 (b), with ε increasing, the correlation then decreases. This is because that a larger contribution of SBCs, can lead to a larger envelope fluctuation of the signal, causing a smaller value of spatial CCFs.

Fig. 5 demonstrates the normalized temporal ACF for (a) different VR SBCs proportion ε and (b) different power contributions η_S. It can be seen that in Fig. 5(a), when the non-stationarity is considered, i.e., the larger ε, the influence of observable SBCs in the environment is obvious which means channel variation becomes slower. In Fig. 5(b), the temporal ACF decreases as the time difference Δt increases. When $\eta_S = 0$, it means only DBCs are considered in the environment, which is modeled in [18]. By setting η_S larger, i.e., with the increasing SBCs, the temporal ACF increases. This is due to the effect of the wide beams caused by SBCs in VR. The non-stationarity increases the beam width of the visible MPCs, causing the power spread to beams nearby. In addition, with both SBCs and DBCs existing in the environment, relatively higher ACF values are observed, which implies that the existing models do not accurately estimate the ACF.

Fig. 6 shows the normalized amplitude contours and MPC angular distribution using a planar antenna array with 64×64 antennas for different VR SBCs proportion ε. For comparison, the marked 'o' and 'x' in Fig. 6(b) represent the MPC angular distribution of the wholly visible and SBCs in VR, respectively. In Fig. 6(a), $\varepsilon = 0$ means that the entire antenna array can be observed by all clusters, which is used in the existing BDCM. In this case, the spatial resolution is large enough to discriminate all MPCs for different directions. In Fig. 6(c), $\varepsilon = 0.8$, considering the influence of SBCs in VR for $\alpha_{sbc} = -\pi/3$, $v_{sbc} = 3m/s$, the spatial resolution corresponding to the VR direction is reduced. For example, in Fig. 6(c), the beam resolution is reduced near position $A_{40,40}$, which corresponds to the VR clusters distributed in the $(20°, 20°)$ direction. The beam near position $A_{55,45}$ becomes no longer visible. The results show that the non-stationarity

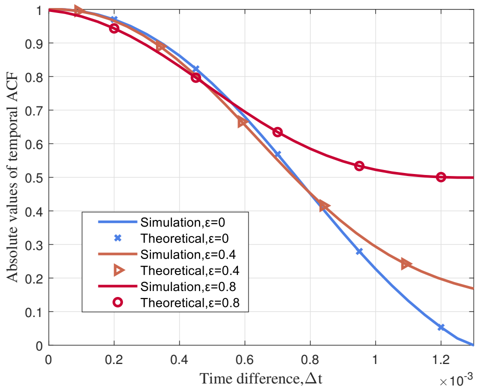

(a)

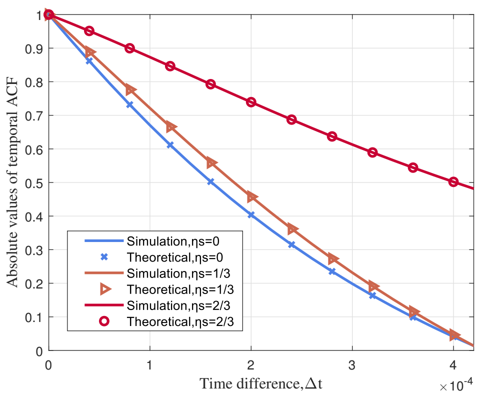

(b)

Fig. 5. ACF for (a) different ε and for (b) different η_S($P_h = P_v = 64$, D=15m, $f_c = 28GHz$, $t = 1s$, $\alpha^T_{m/s} = \beta^T_{n/s} = \frac{\pi}{6}$, $\alpha^R_{m/s} = \beta^R_{n/s} = \frac{\pi}{4}$,$\alpha = \pi/6$, $v = 5m/s$, $\alpha_{sbc} = -\pi/3$, $v_{sbc} = 3m/s$, (a) $\eta_S = 1/3$, $\eta_D = 2/3$, (b) $\varepsilon = 0.4$, NLoS).

of the beam domain channel increases the beam width and decreases the resolution in VR direction, thus affecting the beam richness and resolution.

Fig. 7 shows the channel capacity of different array configurations with different ε. Theoretically, the channel capacity is proportional to the number of antennas, i.e., the array with $M \times M$ antennas has M times higher channel capacity gain than that with the 1×1 antenna method [37]. However, simulation results with two different antenna arrays do not agree with the theoretical results, which can be explained by the rich scattering characteristics of the beam domain channel. Meanwhile, the larger ε for SBCs, the smaller the channel capacity. This is because that the more VR SBCs cause wider beams, and reduce the number of independent beams leading to the lower ergodic capacity of the beam domain channel. The results suggest that the conventional BDCM ignoring the non-stationarity and power contributions of SBCs may result in incorrect estimation of channel capacity.

Fig. 8 depicts the power leakage of the channel. The results show that the power leakage increases with increasing SNR. For instance, in the case of $\varepsilon = 0.2$, nearly 35% of the power is leaked when the SNR is $0dB$, while the leakage increases

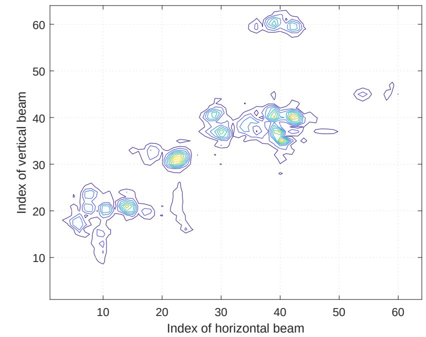

(a)

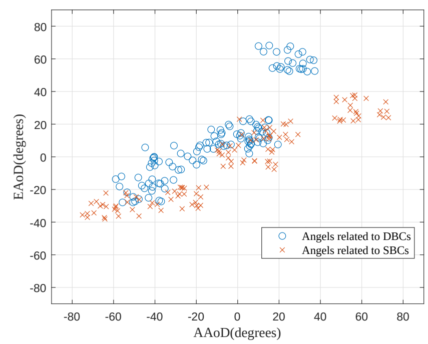

(b)

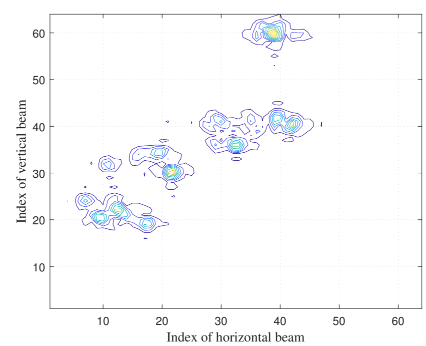

(c)

Fig. 6. Normalized contour plots of $|\boldsymbol{H}_B|$ for (a) $\varepsilon = 0$, (b) angular distribution of MPCs, and (c) $\varepsilon = 0.8$ ($P_h = P_v = 64$, $D = 15m$, $f_c = 28GHz$, $\alpha^T_{m/s} = \beta^T_{n/s} = \frac{\pi}{6}$, $\alpha^R_{m/s} = \beta^R_{n/s} = \frac{\pi}{4}$, $\alpha = \pi/6$, $v = 5m/s$, $\alpha_{sbc} = -\pi/3$, $v_{sbc} = 3m/s$, $t = 1s$, NLoS).

to 60% at $30dB$. It can be seen that the power leakage is up to 90% for $\varepsilon = 0.8$ at arbitrary SNR. In this case, the power leakage becomes relatively severer. The results show that the characteristic of non-stationarity underestimates the power leakage of beam domain channels.

VI. Conclusion

A novel mixed-bouncing BDCM at mmWave bands has been proposed, where both single-bouncing rays and double bouncing-rays have been considered simultaneously. The well fit between the simulated and the measurement results exhibits the correctness of the proposed model. Furthermore, based on the proposed model, the key channel statistical properties have been derived and analyzed, including CCF, ACF, beam spread,

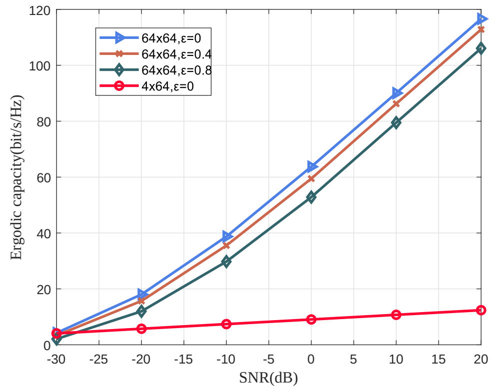

Fig. 7. Ergodic capacity of the proposed BDCM with different ε and array configurations(D=15m, $f_c = 28GHz$, $\alpha^T_{m/s} = \beta^T_{n/s} = \frac{\pi}{6}$, $\alpha^R_{m/s} = \beta^R_{n/s} = \frac{\pi}{4}$, $\alpha = \pi/6$, $v = 5m/s$, $\alpha_{sbc} = -\pi/3$, $v_{sbc} = 3m/s$, NLoS).

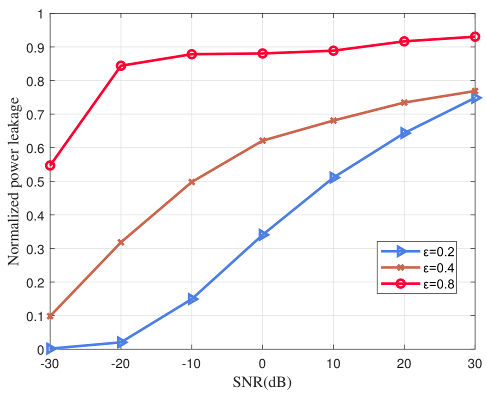

Fig. 8. Power leakage in percentage versus channel power($P_h = P_v = 64$, D=15m, $f_c = 28GHz$, $\alpha^T_{m/s} = \beta^T_{n/s} = \frac{\pi}{6}$, $\alpha^R_{m/s} = \beta^R_{n/s} = \frac{\pi}{4}$, $\alpha = \pi/6$, $v = 5m/s$, $\alpha_{sbc} = -\pi/3$, $v_{sbc} = 3m/s$, NLoS).

channel capacity, and power leakage. The results show that the power ratio and variable VRs of the single-bouncing clusters have a significant impact on the beam domain channel.

However, the proposed model have not take the variations of angles within clusters into account which emphasizes the effect of the single-bouncing clusters on beam domain channel. In the future work, more detailed cluster model can be introduced into BDCM to make it more general for different realistic scenarios, and verify the accuracy of the model compared with measurement data.

References

[1] S. A. Busari, K. M. S. Huq, S. Mumtaz, L. Dai, and J. Rodriguez, "Millimeter-wave massive MIMO communication for future wireless systems: A survey," *IEEE Commun. Surveys Tuts.*, vol. 20, no. 2, pp. 836–869, Dec. 2017.

[2] I. A. Hemadeh, K. Satyanarayana, M. El-Hajjar, and L. Hanzo, "Millimeter-wave communications: Physical channel models, design considerations, antenna constructions, and link-budget," *IEEE Commun. Surveys Tuts.*, vol. 20, no. 2, pp. 870–913, Dec. 2017.

[3] C.-X. Wang, X. You, X. Gao, *et al.*, "On the road to 6G: Visions, requirements, key technologies and testbeds," *IEEE Commun. Surveys Tuts.*, early access, 2023, doi: 10.1109/COMST.2023.3249835.

[4] C.-X. Wang, J. Huang, H. Wang, X. Gao, X.-H. You, and Y. Hao, "6G wireless channel measurements and models: Trends and challenges," *IEEE Veh. Technol. Mag.*, vol. 15, no. 4, pp. 22-32, Dec. 2020.

[5] C.-X. Wang, Z. Lv, X. Gao, X.-H. You, Y. Hao, and H. Haas, "Pervasive wireless channel modeling theory and applications to 6G GBSMs for all frequency bands and all scenarios," *IEEE Trans. Veh. Technol.*, vol. 71, no. 9, pp. 9159-9173, Sept. 2022.

[6] X. Gao, L. Dai, Z. Chen, Z. Wang, and Z. Zhang, "Near-optimal beam selection for beamspace mmWave massive MIMO systems," *IEEE Commun. Lett.*, vol. 20, no. 5, pp. 1054-1057, May. 2016.

[7] P. Amadori and C. Masouros, "Low RF-complexity millimeter-wave beamspace-MIMO systems by beam selection," *IEEE Trans. Commun.*, vol. 63, no. 6, pp. 2212-2222, Jun. 2015.

[8] A. Sayeed and J. Brady, "Beamspace MIMO for high-dimensional multiuser communication at millimeter-wave frequencies," *Proc. IEEE Global Communications Conference (IEEE GLOBECOM' 13)*, pp. 3679-3684. Dec. 2013.

[9] A. Sayeed and N. Behdad, "Continuous aperture phased MIMO: Basic theory and applications," *2010 48th Annual Allerton Conference on Communication, Control, and Computing (Allerton)*, pp. 1196-1203, Sep. 2010.

[10] S. Cui, A. J. Goldsmith, and A. Bahai, "Energy-efficiency of MIMO and cooperative MIMO techniques in sensor networks," *IEEE J. Sel. Areas Commun.*, vol. 22, no. 6, pp. 1089-1098, Aug. 2004.

[11] S. Han, C. L. I, Z. Xu, Q. Sun and H. Li, "Large-scale antenna systems with hybrid precoding analog and digital beamforming for millimeter wave 5G," *IEEE Commun. Mag.*, vol. 53, no. 1, pp. 186-194, Jan. 2015.

[12] J. Wang, C.-X. Wang, J. Huang, H. Wang, and X. Q. Gao, "A general 3D space-time-frequency non-stationary THz channel model for 6G ultra-massive MIMO wireless communication systems," *IEEE J. Sel. Areas Commun.*, vol. 39, no. 6, pp. 1576–1589, Jun. 2021.

[13] N. Al-Falahy and O. Y. K. Alani, "Millimetre wave frequency band as a candidate spectrum for 5G network architecture: A survey," *Phys. Commun.*, vol. 32, pp. 120–144, Feb. 2019.

[14] Y. Zeng and R. Zhang, "Millimeter wave MIMO with lens antenna array:A new path division multiplexing paradigm," *IEEE Trans. Commun.*, vol. 64, no. 4, pp. 1557-1571, Apr. 2016.

[15] J. Brady, N. Behdad, and A. M. Sayeed, "Beamspace MIMO for millimeter-wave communications: System architecture, modeling, analysis, and measurements," *IEEE Trans. Antennas Propag.*, vol. 61, no. 7, pp. 3814–3827, Jul. 2013.

[16] A. Sayeed and J. Brady, "Beamspace MIMO Channel Modeling and Measurement: Methodology and Results at 28GHz," *2016 IEEE Globecom Workshops (GC Wkshps)*, pp. 1-6, Dec. 2016.

[17] Y. Chen, G. Li, C. Sun, J. Zhang, E. Jorswieck and B. Xiao, "Beam-Domain Secret Key Generation for Multi-User Massive MIMO Networks," *ICC 2020 - 2020 IEEE International Conference on Communications (ICC), Dublin, Ireland*, pp. 1-6. Jun. 2020.

[18] X. Xia, K. Xu, D. Zhang, Y. Xu and Y. Wang, "Beam-Domain Full-Duplex Massive MIMO: Realizing Co-time Co-frequency Uplink and Downlink Transmission in the Cellular System," *IEEE Trans. Veh. Technol.*, vol. 66, no. 10, pp. 8845-8862, Oct. 2017.

[19] F. Lai, C.-X. Wang, J. Huang, X. Gao and F. C. Zheng, "A Novel Massive MIMO Beam Domain Channel Model," *2020 IEEE Wireless Communications and Networking Conference (WCNC)*, pp. 1-6. May. 2020.

[20] J. Bian, C.-X. Wang, R. Feng, *et al.*, "A Novel 3D Beam Domain Channel Model for Massive MIMO Communication Systems." *IEEE Trans. Wireless Commun.*, early access, 2022, doi: 10.1109/TWC.2022.3205929.

[21] C. Ling, X. Yin, R. Müller, *et al.*, "Double-Directional Dual-Polarimetric Cluster-Based Characterization of 70–77 GHz Indoor Channels," *IEEE Trans. Antennas Propag.*, vol. 66, no. 2, pp. 857-870, Feb. 2018.

[22] S. Kishimoto, M. Kim, D. He and K. Guan, "Scattering Process Identification and Cluster Analysis for Millimeter-wave Indoor Channel Model," *2018 International Symposium on Antennas and Propagation (ISAP), Busan, Korea (South)*, 2018, pp. 1-2.

[23] C. Liu, M. Li, S. V. Hanly, I. B. Collings and P. Whiting, "Millimeter Wave Beam Alignment: Large Deviations Analysis and Design Insights," *IEEE J. Sel. Areas Commun.*, vol. 35, no. 7, pp. 1619-1631, Jul. 2017.

[24] B. Wang, X. Li, F. Gao and G. Y. Li, "Power Leakage Elimination for Wideband mmWave Massive MIMO-OFDM Systems: An Energy-Focusing Window Approach," *IEEE Trans. Signal Process.*, vol. 67, no. 21, pp. 5479-5494, 1, Nov. 2019.

[25] I. Khaled, C. Langlais, A. El Falou, M. Jezequel and B. ElHassan, "Joint Single- and Multi-Beam Angle-Domain NOMA for Hybrid MmWave MIMO Systems," *WSA 2021; 25th International ITG Workshop on Smart Antennas, French Riviera, France*, pp. 1-6, Nov. 2021.

[26] N. Ye, X. Li, J. Pan, W. Liu and X. Hou, “Beam Aggregation-Based mmWave MIMO-NOMA: An AI-Enhanced Approach,” *IEEE Trans. Veh. Technol.*, vol. 70, no. 3, pp. 2337-2348, Mar. 2021.

[27] H. Zhang, N. Shlezinger, F. Guidi, D. Dardari, M. F. Imani and Y. C. Eldar, “Beam Focusing for Near-Field Multiuser MIMO Communications,” *IEEE Trans. Wireless Commun.*, vol. 21, no. 9, pp. 7476-7490, Sep. 2022.

[28] L. You, X. Gao, G. Y. Li, X. G. Xia and N. Ma, “BDMA for Millimeter-Wave/Terahertz Massive MIMO Transmission With Per-Beam Synchronization,” *IEEE J. Sel. Areas Commun.*, vol. 35, no. 7, pp. 1550-1563, Jul. 2017.

[29] X. Gao, J. Flordelis, G. Dahman, F. Tufvesso, and O. Edfors, “Massive MIMO channel modeling — extension of the COST 2100 model,” *Proc. JNCW’ 15, Barcelona, Spain*, pp. 380–394, Oct. 2015.

[30] H. Chang, C.-X. Wang, J. Bian, *et al.*, “A Novel 3D Beam Domain Channel Model for UAV Massive MIMO Communications,” *IEEE Trans. Wireless Commun.*, early access, 2023, doi: 10.1109/TWC.2023.3233961.

[31] L. Bai, Z. Huang, L. Cui, T. Feng and X. Cheng, “A Mixed-Bouncing Based Non-Stationary Model for 6G Massive MIMO mmWave UAV Channels,” *IEEE Trans Commun*, vol. 70, no. 10, pp. 7055-7069, Oct. 2022.

[32] 3GPP TR 38.901, V14.0.0, “Study on channel model for frequencies from 0.5 to 100 GHz (Release 14),” Mar. 2017.

[33] Z. Pi and F. Khan, “An introduction to millimeter-wave mobile broadband systems,” *IEEE Commun. Mag.*, vol. 49, no. 6, pp. 101–107, Jun. 2011.

[34] T. S. Rappaport, S. Sun, R. Mayzus, *et al.*, “Millimeter wave mobile communications for 5G cellular: It will work!” *IEEE Access*, vol. 1, pp. 335–349, May. 2013.

[35] J. Bian, C.-X. Wang, X. Gao, X. You, and M. Zhang, “A general 3D non-stationary wireless channel model for 5G and beyond,” *IEEE Trans. Wireless Commun.*, vol. 20, no. 5, pp. 211–3224, May. 2021.

[36] P. Kyösti *et al.*, “WINNER II channel models,” *IST-WINNER D1.1.2 ver1.1*, Sep. 2007.

[37] P. Amadori and C. Masouros, “Low RF-complexity millimeter-wave beamspace-MIMO systems by beam selection,” *IEEE Trans. Commun.*, vol. 63, no. 6, pp. 2212-2222, Jun. 2015.

[38] M. Patzold, *Mobile Radio Channels*, 2nd ed. West Sussex, U.K.: Wiley, 2012.

[39] J. Li, B. Ai, R. He, M. Yang, Z. Zhong, Y. Hao, and G. Shi, “On 3D cluster-based channel modeling for large-scale array communications.” *IEEE Trans. Wireless Commun.*, vol. 18, no. 10, pp. 4902–4914, Oct. 2019.

[40] T. Xie, L. Dai, D. W. K. Ng, and C. B. Chae, “On the power leakage problem in millimeter-wave massive MIMO with lens antenna arrays,” *IEEE Trans. Signal Process.*, vol. 67, no. 18, pp. 4730–4744, Sep. 2019.

[41] A. G. Zajić and G. L. Stüber, “Three-dimensional modeling and simulationof wideband MIMO mobile-to-mobile channels,” *IEEE Trans. Wireless Commun.*, vol. 8, no. 3, pp. 1260–1275, Mar. 2009.

[42] J. Li, B. Ai, R. He, M. Yang, Z. Zhong, and Y. Hao, “A cluster-based channel model for massive MIMO communications in indoor hotspot scenarios,” *IEEE Trans. Wireless Commun.*, vol. 18, no. 8, pp. 3856–3870, Aug. 2019.

Hao Qian was born in Zhangjiagang, Jiangsu, China, in 1997. He received the B.S. degree from Jiangnan University, Wuxi, Jiangsu, China, in 2020. He is currently studying for the M.S. degree in the School of Internet of Things Engineering, Jiangnan University, Wuxi, Jiangsu, China. His research interest is beam domain channel model and wireless propagation.

Yang Liu (M′18) was born in Wuxi, Jiangsu, China, in 1988. He received the Ph.D. degree in communication and information system from Key Laboratory of Wireless Communication, Nanjing University of Posts and Telecommunications (NUPT), Nanjing, China, in 2016. He is currently an associate Professor in Institute of IOT Engineering, Jiangnan Univer sity, Wuxi, Jiangsu. He has authored and co-authored over 10 technical papers published in peer-reviewed international journals and conference proceedings. His research interests include the wireless channel modeling and network coding.

Cheng−Xiang Wang (Fellow, IEEE) received the B.Sc. and M.Eng. degrees in communication and information systems from Shandong University, China, in 1997 and 2000, respectively, and the PhD.degree in wireless communications from Aalborg University, Denmark, in 2004. He was a Research Assistant with the Hamburg University of Technology, Hamburg, Germany, from 2000 to 2001; a Visiting Researcher with Siemens AG Mobile Phones, Munich, Germany, in 2004; and a Research Fellow with the University of Agder, Grimstad, Norway, from 2001 to 2005. He has been with Heriot-Watt University, Edinburgh, U.K., since 2005, where he was promoted to a Professor in 2011. In 2018, he joined Southeast University, Nanjing, China, as a Professor. He is also a part-time Professor with Purple Mountain Laboratories, Nanjing. He has authored 4 books, 3 book chapters, and more than 490 papers in refereed journals and conference proceedings, including 26 highly cited papers. He has also delivered 24 invited keynote speeches/talks and tentutorials in international conferences. His current research interests include wireless channel measurements and modeling, 6G wireless communication networks, and electromagnetic information theory.

Rui Feng (Member, IEEE) received the B.Sc. degree in Communication Engineering from Yantai University, China, in 2011, the M.Eng. degree in Signal and Information Processing from Yantai University, China, in 2014, and the Ph.D. degree in Communication and Information System from Shandong University, China, in 2018. From July 2018 to Sept. 2020, she was a lecture in Ludong University, China. She is currently a Postdoctoral Research Associate in Purple Mountain Laboratories and Southeast University, China. Her research interests include (ultra-) massive MIMO channel modeling theory and beam domain channel modeling.

Wen−Jun Lu (Senior Member, IEEE) received Ph.D degree in electronic engineering from the Nanjing University of Posts and Telecommunications (NUPT), Nanjing, China, in 2007. He has been a Professor with the Jiangsu Key Laboratory of Wireless Communications, NUPT, since 2013. He has authored or co-authored over 180 technical papers published in peer-reviewed international journals and conference proceedings. He is the translator of the Chinese version The Art and Science of Ultrawideband Antennas (by H. Schantz). He has authored the book Antennas: Concise Theory, Design and Applications (in Chinese). His research interests include antenna theory, antenna/array designs, wireless propagation and channel modelling. He was a recipient of the Exceptional Reviewers Award of the IEEE TRANSACTIONS ON ANTENNAS AND PROPAGATION in 2016. He has been serving as an Editorial Board Member of the International Journal of RF and Microwave Computer-Aided Engineering since 2014. He has been serving as an Associate Editor of Electronics Letters since 2019.

Hong−Bo Zhu (Member, IEEE) was born in Yangzhou, China, in 1956. He is currently the standing Director of the Chinese Institute of Electronics and the Director of the Jiangsu Key Laboratory of Wireless Communications, Nanjing University of Posts and Telecommunications. He has authored and co-authored over 100 journal papers and over 60 invention patents authorized. In the past five years, he has undertaken over 30 projects at the national, provincial and ministerial level. His research interests include wireless communications, Internet of Things, and EMC.